This is a repository copy of *Towards a micro-kinetic model of Li-Ion battery thermal runaway - reaction network analysis of dimethyl carbonate thermal decomposition*.

White Rose Research Online URL for this paper:
https://eprints.whiterose.ac.uk/201283/

Version: Published Version

Article:
Bugryniec, P. orcid.org/0000-0003-3494-5646, Vernuccio, S. and Brown, S. orcid.org/0000-0001-8229-8004 (2023) Towards a micro-kinetic model of Li-Ion battery thermal runaway - reaction network analysis of dimethyl carbonate thermal decomposition. Journal of Power Sources, 580. 233394. ISSN 0378-7753

https://doi.org/10.1016/j.jpowsour.2023.233394

Reuse
This article is distributed under the terms of the Creative Commons Attribution (CC BY) licence. This licence allows you to distribute, remix, tweak, and build upon the work, even commercially, as long as you credit the authors for the original work. More information and the full terms of the licence here: https://creativecommons.org/licenses/

Takedown
If you consider content in White Rose Research Online to be in breach of UK law, please notify us by emailing eprints@whiterose.ac.uk including the URL of the record and the reason for the withdrawal request.

eprints@whiterose.ac.uk
https://eprints.whiterose.ac.uk/

Journal of Power Sources 580 (2023) 233394

Contents lists available at ScienceDirect

Journal of Power Sources

journal homepage: www.elsevier.com/locate/jpowsour

Towards a micro-kinetic model of Li-ion battery thermal runaway — Reaction network analysis of dimethyl carbonate thermal decomposition

Peter J. Bugryniec, Sergio Vernuccio, Solomon F. Brown *

Department of Chemical & Biological Engineering, The University of Sheffield, Sheffield, S1 3JD, UK

HIGHLIGHTS

- Micro-kinetic modelling applied to Li-ion battery thermal runaway predictions.
- Two reaction networks of DMC thermal decomposition compared.
- Radical species play a critical role in allowing accurate predictions at low temperatures.
- Degree of rate control applied to reduce network complexity.
- Proposal of a method to allow for predictive hazard assessment of flammable gases.

GRAPHICAL ABSTRACT

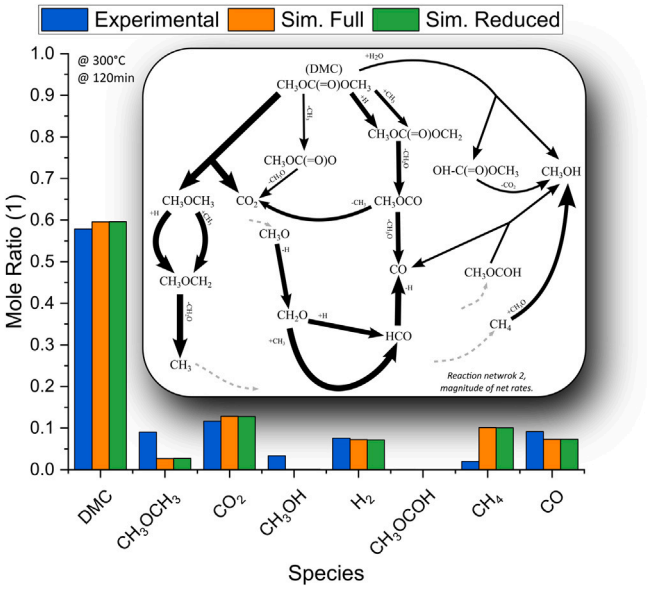

ARTICLE INFO

Keywords:
Density functional theory
Electrolyte
Degradation
Fire safety
Gas composition

ABSTRACT

Thermal runaway (TR), a major safety concern for Li-ion batteries (LIBs), involves a complex network of chemical reactions leading to the production of flammable and toxic gases. Computational modelling of LIB TR continues to aid safer battery design. But to improve the capability of TR simulations, here we apply micro-kinetic modelling to describe the kinetics of LIB TR at a mechanistic level. We focused on developing a micro-kinetic model for the thermal decomposition of dimethyl carbonate, an important electrolyte component. Comparing two reaction networks for this process, (1) not involving radical pathways and (2) involving radical pathways, we show that radical reaction pathways are important for the decomposition of DMC at low temperatures in the region of TR onset. Further, this second network is important for the accurate prediction of off-gas species. This work forms the basis of being able to predict hazardous species production. With further work to develop a reaction network for the decomposition of the entire electrolyte and electrode-electrolyte reactions, predictive capabilities can be extended to allow for detailed risk assessment of LIBs.

* Corresponding author.
E-mail address: s.f.brown@sheffield.ac.uk (S.F. Brown).

https://doi.org/10.1016/j.jpowsour.2023.233394
Received 20 March 2023; Received in revised form 13 June 2023; Accepted 5 July 2023
Available online 26 July 2023
0378-7753/© 2023 The Author(s). Published by Elsevier B.V. This is an open access article under the CC BY license (http://creativecommons.org/licenses/by/4.0/).

1. Introduction

Lithium-ion batteries (LIBs) are at the forefront of electrochemical energy storage devices utilised in electric vehicles and grid-scale applications. The performance, cost and safety of LIBs has continually improved over their lengthy commercial history [1,2], but fires and explosions are still apparent within battery failure due to thermal runaway (TR) [3–5]. During TR a series of exothermic decomposition reactions increases the battery's temperature exponentially and leads to the release of flammable gases [6–8].

Assessment of LIB safety and the TR process has been investigated experimentally and computationally. TR decomposition reaction modelling has been extensively used for safety analysis of LIBs and packs through predictions of temperature rise and heat transfer, and more recently the predictions of pressure build-up and flammability behaviour [for example, 9–15]. These modelling approaches typically consist of lumping several reactions into a single step which is governed by an overall rate constant describing the thermal decomposition of the cell's materials. Although effective in describing the kinetics of the process, this approach has several limitations as it does not (1) consider the multiple and interdependent reaction pathways within, and between, cell materials, nor (2) have the ability to predict the concentration profiles of real decomposition products and reaction intermediates.

The first point is important as the decomposition products from one reaction can be influential in another, for example, most notably, the generation of oxygen that can lead to the combustion of the electrolyte [6,7]. Addressing the second point enables the capability to predict the chemical and fire/explosion hazard from the gases produced, allowing for quantitative risk assessments. Further, the predictive power of these simplified models is usually limited within the ranges of experimental conditions to which the rate constants were fit. To overcome these simplifications, a realistic representation of the chemical reaction network of LIB decomposition during TR is desired. Herein we apply microkinetic modelling and chemical reaction network analysis to meet this goal.

In microkinetic modelling an overall chemical reaction is defined by a set of relevant elementary reaction steps that make up the edges and pathways of the network, while the species represent the nodes of the network. These elementary reaction steps are governed by elementary rate equation laws which respect the microscopic reversibility (i.e. each elementary step can proceed in both forward and reverse direction over the same transition state) [16]. Kinetic parameters can be estimated from quantum chemistry calculations, based on density functional theory (DFT), and transition state theory [17]. A detailed description of the reaction pathways including products and reaction intermediates is realised due to the mechanistic nature of microkinetic modelling. In addition, in the microkinetic modelling approach, the number of *a priori* assumptions is significantly limited and the kinetic parameters have a fundamental nature [16,18]. Analysis of large and interconnected reaction networks undertaken through the use of the microkinetic model, calculating the rates of each elementary step, eludes the identification of the dominant reaction pathways and intermediary species. Further, the application of Gaussian Processes (i.e. machine learning techniques) can help identify the most dominant reaction parameters and be used to develop efficient reduced-order models of the complex microkinetic models [19].

The anode, cathode and electrolyte are the main active components in normal battery operation, but also contribute to TR. The electrolyte, which allows the transfer of Lithium-ions between the cathode and anode [7,20], is commonly a non-aqueous solution of lithium salts dissolved in a binary or tertiary mixture of carbonate solvents [20–23]. These solvents are highly flammable and contribute significantly (~50%) to the energy released during TR [24–26]. As such they are the main focus of this work. Typical solvents include dimethyl carbonate (DMC), ethyl methyl carbonate (EMC), diethyl carbonate (DEC), propylene carbonate (PC) and ethylene carbonate (EC), while the most common salt used is lithium hexafluorophosphate. Decomposition of the solvents within a LIB can occur via thermal decomposition, reduction on the anode or oxidation on the cathode [24].

DMC (in gas and liquid phases) is reported to be one of the most stable electrolyte solvents not decomposing until 350°C [27,28]. In the liquid case by Lamb et al. [28] the lack of decomposition was hypothesised to potentially have been due to the vaporisation of the DMC consuming the energy that would otherwise been used for decomposition.

However, contrary to this, similar experiments of DMC decomposed on quartz have shown reactions occur at 257°C producing CO_2 and CH_3OCH_3, with a calculated apparent activation barrier of $17\,kcal\,mol^{-1}$ [29]. Further, Wijnen [29] found that methanol was formed by hydrolysis and that the increase in methanol also coincided with an increase in carbon dioxide. Similarly, Thynne and Gray [30] report that the decomposition of DMC in the gas phase over the temperature range of 150°C to 240°C occurs with an activation barrier of $15\,kcal\,mol^{-1}$. Thynne and co-authors further report that the methyl radical-sensitised decomposition of DMC has an activation barrier of $7.4\,kcal\,mol^{-1}$ to $8.9\,kcal\,mol^{-1}$ [30,31]. Products of DMC decomposition by photolysis include methanol (CH_3OH), carbon monoxide, carbon dioxide, methane (CH_4), dimethyl ether (CH_3OCH_3), methyl ethyl ether ($CH_3OCH_2CH_3$), and traces of methyl formate ($HC(O)OCH_3$).

Fernandes et al. [32] injected DMC into a heated stainless steel vessel and monitored the production of gas species. Firstly, DSC showed DMC decomposed at 247°C (with linear solvents such as DMC decomposing before cyclic solvents e.g EC). The steel vessel was heated over a 2 h period at 180°C, 240°C and 300°C. At 180°C the decomposition products were primarily CO_2, CH_3OH, and CH_3OCH_3 with small quantities of $CH_3OC(=O)H$ and H_2. At 240°C, CO and a small amount of CH_4 were detected, with an increase in the production of H_2. At 300°C greater amounts of CO and H_2 were produced (on the scale of CH_3OCH_3), with a reduction in CH_3OH.

At substantially higher temperatures (>800°C), in pyrolysis experiments DMC decomposition leads to CO, CO_2 and CH_4 being predominately produced, followed by DME, C_2H_4 and C_2H_6, with small amounts of C_2H_2 [33]. Further, CO is produced after CO_2, and fuel-related reactions lead to CO_2 but CO is produced by reactions with small molecules. A large amount of CO_2 is produced because the radical CH_3OCO easily decomposes to CO_2 and CH_3. Almost all of the CO_2 is originated from DMC $\longrightarrow$ $CO_2 + CH_3OCH_3$ (and is more significant at lower temperatures), CH_3OCO $CH_3OCO \longrightarrow CH_3 + CO_2$ and $CH_3OC(=O)O \longrightarrow CH_3O + CO_2$. Similar experiments show the same species generation as Sun et al. [33] except with H_2 being produced on a comparable scale of CO and with no DME detected [34].

The possible primary thermal decomposition reactions of DMC are listed in (R1) to (R8) [29,31,35]. The bond fission reaction (R2), (R5) and (R6) and ultimately lead to CH_3, CO_2, CH_2O, and H at high temperatures [35]. The micro-kinetic models of the high temperature pyrolysis experiments show that reaction (R1) is the most favourable followed by reaction (R2) [33]. Similarly for shock-tube experiments, modelling shows that reaction (R1) is the dominant decomposition channel, with an activation barrier of $71\,kcal\,mol^{-1}$ [35], while reactions (R2) to (R4) are kinetically insignificant with activation energies $21\,kcal\,mol^{-1}$ greater than reaction (R1). Also, the activation energy of reaction (R1) was determined to be $69.8\,kcal\,mol^{-1}$ using CBS-Q methods with geometries optimised at the B3LYP/6-31G(d,p) method and basis set [36].

$$CH_3OC(O)OCH_3 \longrightarrow CO_2 + CH_3OCH_3 \quad (R1)$$

$$\longrightarrow CH_3 + CH_3OC(O)O \quad (R2)$$

$$\longrightarrow CH_3OCOH + CH_2O \quad (R3)$$

$$\longrightarrow H_2 + CH_3OC(O)OCH \quad (R4)$$

$$\longrightarrow H + CH_2OC(O)OCH_3 \quad (R5)$$

$$\longrightarrow CH_3O + COOCH_3 \quad \text{(R6)}$$

$$\longrightarrow 2\,CH_3O + CO \quad \text{(R7)}$$

$$\longrightarrow CH_3 + CO_2 + CH_3O \quad \text{(R8)}$$

DFT studies have been used within LIB chemistry analysis to elucidate the decomposition behaviour of electrolytes. For example, to investigate the oxidation pathways of EC [37], the reduction of cyclic solvents [38], the generation of the solid electrolyte interphase [39], and the effect of $LiPF_6$ salt on solvent stability [40]. Network analysis studies have been carried out on the oxidative decomposition of EC [37,41]. Five pathways for the one-electron oxidation of EC were postulated by Xing et al. [37], showing that CO_2 is more easily formed than CO due to the high activation energies of the pathways that lead to CO formation. For the one-electron oxidation of EC, an automated reaction network generation method identified 203 reactions and 42 species [41]. From this, a more energetically favourable pathway to CO_2 production was identified, via a bimolecular EC reaction compared to single EC oxidation. Also, kinetic models have been developed [33,34,36,42,43] and compared against experimental data [34] to elucidate the DMC decomposition at high temperatures.

To prevent TR from developing into a serious event it is important to understand the initial decomposition of battery components at low temperatures that are characteristic of the TR onset temperatures of LIB's. A reaction scheme has been proposed to explain the generated reaction products from DMC electrolyte decomposition at low temperatures [32] however this has not been validated. Further, as stated above, the literature on the decomposition of DMC is contradictory, hence it is of interest to investigate the possible reaction network of low-temperature decomposition.

In this work, we aim to develop a microkinetic model of DMC TR. This represents the first step towards the development of a general microkinetic model describing the TR of LIB, as a similar approach can be extended to other components of the electrolyte. We investigate the thermal decomposition process at a low temperature (180°C to 300°C) that is in the region of TR onset. We examine two reaction networks proposed in the literature and apply DFT to determine the kinetic parameters governing the process. The model is then refined by optimising the kinetic parameters within ranges dictated by theory and then validated against available experimental data. From this, a discussion of the thermal decomposition of DMC is made.

2. Methodology

Within the Methodology, Section 2.1 first introduces the DFT calculations used to determine the thermochemistry of the reaction complexes. Section 2.2 describes the microkinetic modelling theory used to govern the simulation of the reaction network. Section 2.3 presents the reaction systems studied for the thermal decomposition of DMC. Section 2.4 outlines the optimisation procedure used to determine optimal reaction kinetic parameters. Finally, Section 2.5 describes the methods used to analyse the reaction network to understand the network behaviour and determine the important reaction steps.

2.1. DFT calculations

Quantum mechanical calculations were carried out using *Gaussian 16* computational chemistry software [44]. The geometries of the reaction species, complexes and transition state (TS) structures were optimised using density functional theory (DFT) with the method and basis set combination of B3LYP/6-311++G(d,p). This method and basis set was used following similar work in the literature [see 35,37,45,46]. The activation energy of reaction (R1), calculated here to be 65 kcal mol^{-1}, was benchmarked against Zhang et al. [47] who determined it to be 68 kcal mol^{-1}. Frequency analysis was carried out on all structures to verify that equilibrium structures had entirely real frequencies and that each TS had a single imaginary frequency. To validate each TS an intrinsic reaction coordinate (IRC) calculation was carried out. The frequency analysis was also used to determine the zero point energy (ZPE) corrections, enthalpy and Gibbs free energy of the structures at 298.15 K and 1 atm. Both the frequency analysis' and IRC calculations were carried out at the level B3LYP/6-311++G(d,p). Note, for reactions that involve radical recombinations wherein the stable structure of the complex could not be found, the thermochemistry is then determined as the sum of the separate radical energies. The output text files containing the optimised geometries are supplied in the *Supplementary Data — Optimised Geometries*.

2.2. Microkinetic modelling

The rate constant, k (s^{-1} or $L\,s^{-1}\,mol^{-1}$ for unimolecular and bimolecular reactions respectively), of each elementary step is governed by an Arrhenius equation of the form [18]

$$k = Ae^{-E_a/RT} \quad (1)$$

where A is the pre-exponential factor (s^{-1}) or ($L\,s^{-1}\,mol^{-1}$), E_a is the activation energy ($J\,mol^{-1}$), R is the universal gas constant ($J\,K^{-1}\,mol^{-1}$), T is the temperature (K). The activation energies and pre-exponential factors were estimated using transition state theory [48], following Eqs. (2) and (3) respectively.

$$E_a = \Delta H^{\ddagger} + nRT \quad (2)$$

$$A = \left(\frac{k_b T}{h}\right) e^{\Delta S^{\ddagger}/R} e^{1-\Delta n^{\ddagger}} \left(c^0\right)^{\Delta n^{\ddagger}} \quad (3)$$

where, $\Delta H^{\ddagger}$ ($J\,mol^{-1}$) is the enthalpy of activation, n (1) is the molecularity of the reaction, k_B is Boltzmann's constant ($J\,K^{-1}$), h is Planck's constant ($J\,s^{-1}$), $\Delta S^{\ddagger}$ is the entropy of activation, $\Delta n^{\ddagger}$ (1) is the change in the number of molecules in forming the transition state, and c^0 is the standard state concentration (1 M). Furthermore, the enthalpy of activation is the difference between the enthalpies of the transition state (H_{TS}) and reactants (H_r), i.e. $\Delta H^{\ddagger} = H_{TS} - H_r$. Analogously, the enthalpy of reaction is the difference between the enthalpy of products (H_p) and reactants, see Eq. (7). The enthalpy of each species is obtained as:

$$H = \text{electronic energy} + \text{ZPE} + E_{rot} + E_{trans} + E_{vib} + RT \quad (4)$$

where ZPE is the zero-point energy; and E_{rot}, E_{trans} and E_{vib} are the rotational, translational and vibrational energies respectively.

For thermodynamic consistency the activation energies in the forward and backward directions were imposed to satisfy [49]:

$$E_{a,f} - E_{a,b} = \Delta H_{rxn} + \Delta nRT \quad (5)$$

and the pre-exponential factors should satisfy [50]:

$$\ln\left(A_f / A_b\right) = \Delta S_{rxn}/R \quad (6)$$

where ΔH_{rxn} is the reaction enthalpy (see Eq. (7)), ΔS_{rxn} is the reaction entropy, and the subscripts f and b refer to the forward and backward reactions respectively [50].

$$\Delta H_{rxn} = H_p - H_r \quad (7)$$

The reaction entropy is determined from the Gibbs free energy of the reaction, ΔG_{rxn} ($J\,mol^{-1}$) [50]:

$$\Delta G_{rxn} = \Delta H_{rxn} - T\Delta S_{rxn} \quad (8)$$

where ΔG_{rxn} is calculated from the difference in Gibbs free energy of the stationary point product and reactant complexes [50]:

$$\Delta G_{rxn} = G_p - G_r \quad (9)$$

The micro-kinetic model is computed as a system of n ordinary differential equations (ODEs) describing the change in concentration

Table 1
Reactions considered in the networks, with corresponding kinetics data determined from DFT calculations. Note: Units of A_f depend on the molecularity of reaction. Radical recombination reactions (R27, R33 and R35) are considered to be barrierless, i.e. $\Delta H_f^{\ddagger} = 0$.

Reaction №	Reaction	$\Delta H_f^{\ddagger}$ (J mol^{-1})	A_f (s^{-1}) or (L s^{-1} mol^{-1})	ΔH_{rxn} (J mol^{-1})	ΔS_{rxn} (J mol^{-1} K^{-1})	Notes
1	$CH_3OC(=O)OCH_3 \longrightarrow CO_2 + CH_3OCH_3$	2.71×10^5	3.37×10^{14}	-3.30×10^4	52.21	RN1, [32]
2	$CH_3OC(=O)OCH_3 + H_2O \longrightarrow CH_3OH + OH-C(=O)OCH_3$	2.20×10^5	2.52×10^{10}	-1.66×10^4	−50.61	RN1, [32]
3	$OH-C(=O)OCH_3 \longrightarrow CO_2 + CH_3OH$	1.59×10^5	1.62×10^{14}	-2.71×10^4	67.67	RN1, [32]
4	$CH_3OC(=O)OCH_3 + H_2 \longrightarrow CH_3OH + CH_3OC(=O)H$	2.95×10^5	1.74×10^{10}	-1.93×10^4	−1.05	RN1, [32]
5	$CH_3OCH_3 \longrightarrow CH_4 + CH_2O$	3.09×10^5	1.30×10^{15}	-7.78×10^3	114.25	RN1, [32]
6	$CH_2O \longrightarrow H_2 + CO$	3.35×10^5	1.38×10^{14}	1.47×10^4	38.93	RN1, [32]
7	$CH_3OCH_3 \longrightarrow CH_3 + CH_3O$	3.12×10^5	1.00×10^{10}	3.12×10^5	176.01	RN1
8	$CH_3 + CH_3O \longrightarrow CH_4 + CH_2O$	1.23×10^5	2.91×10^5	-3.20×10^5	−61.76	RN1
9	$CH_3OC(=O)H \longrightarrow CO_2 + CH_4$	3.03×10^5	2.05×10^{15}	-1.17×10^5	114.74	RN1, [32]
10	$CH_3OC(=O)H \longrightarrow CH_3OH + CO$	2.74×10^5	1.08×10^{15}	5.38×10^4	78.43	RN1, [32]
11	$CH_3OC(=O)H \longrightarrow CH_2O + CH_2O$	4.76×10^5	7.14×10^{13}	1.22×10^5	69.68	RN1, [32]
12	$CH_3OH \longrightarrow CH_2O + H_2$	3.68×10^5	5.85×10^{13}	8.69×10^4	61.49	RN1, [32]
13	$CH_3OH \longrightarrow HCOH + H_2$	3.56×10^5	9.95×10^{13}	3.05×10^5	32.87	RN1, [32]
14	$CH_3OC(=O)H \longrightarrow CH_2O + HCOH$	4.30×10^5	2.36×10^{14}	3.16×10^5	35.32	RN1, [32]
15	$HCOH \longrightarrow CH_2O$	1.28×10^5	1.17×10^{14}	-2.20×10^5	−0.63	RN1, [32]
16	$CO_2 + H_2 \longrightarrow H_2O + CO$	4.75×10^5	9.46×10^{10}	6.04×10^4	16.83	RN1
17	$CH_3OC(=O)OCH_3 \longrightarrow CH_3OC(=O)O + CH_3$	3.40×10^5	1.74×10^{14}	3.24×10^5	178.59	RN2, [33]
18	$CH_3OC(=O)OCH_3 + CH_3 \longrightarrow CH_3OC(=O)OCH_2 + CH_4$	4.32×10^4	6.52×10^9	-2.43×10^4	33.45	RN2, [33]
19	$CH_3OC(=O)OCH_3 + H \longrightarrow CH_3OC(=O)OCH_2 + H_2$	1.60×10^4	7.23×10^9	-2.95×10^4	15.77	RN2, [33]
20	$CH_3OC(=O)O \longrightarrow CH_3O + CO_2$	4.65×10^4	3.38×10^{14}	-4.02×10^4	79.30	RN2, [33]
21	$CH_3OC(=O)OCH_2 \longrightarrow CH_2O + CH_3OCO$	1.26×10^5	6.27×10^{14}	7.59×10^4	64.13	RN2, [33]
22	$CH_3OCO \longrightarrow CH_3 + CO_2$	1.13×10^5	2.15×10^{14}	-9.07×10^4	93.44	RN2, [33]
23	$CH_3OCO \longrightarrow CH_3O + CO$	8.29×10^4	3.42×10^{14}	6.68×10^4	77.09	RN2, [33]
24	$CH_3OCH_3 + H \longrightarrow CH_3OCH_2 + H_2$	2.90×10^3	4.29×10^{11}	-4.49×10^4	25.19	RN2, [33]
25	$CH_3OCH_3 + CH_3 \longrightarrow CH_3OCH_2 + CH_4$	3.70×10^4	2.15×10^{10}	-3.84×10^4	30.58	RN2, [33]
26	$CH_3O \longrightarrow H + CH_2O$	1.13×10^5	2.76×10^{14}	1.08×10^5	67.48	RN2, [33]
27	$H + CH_2O \longrightarrow HCO + H_2$	0.00	1.03×10^{11}	-7.49×10^4	23.21	RN2, [33]
28	$CH_2O + CH_3 \longrightarrow HCO + CH_4$	1.73×10^4	4.41×10^{11}	-6.88×10^4	56.02	RN2, [33]
29	$HCO \longrightarrow H + CO$	9.03×10^4	5.41×10^{14}	8.92×10^4	110.34	RN2, [33]
30	$HCO + H \longrightarrow CO + H_2$	8.06×10^4	1.43×10^8	-3.45×10^5	−75.58	RN2, [33]
31	$HCO + CH_3 \longrightarrow CO + CH_4$	1.47×10^5	3.89×10^6	-3.38×10^5	−37.83	RN2, [33]
32	$CH_3OCH_2 \longrightarrow CH_2O + CH_3$	9.04×10^4	6.62×10^{14}	3.15×10^4	81.76	RN2, [33]
33	$CH_4 + OH \longrightarrow CH_3 + H_2O$	0.00	1.99×10^{11}	-5.03×10^4	0.87	RN2, [33]
34	$CH_4 + CH_3O \longrightarrow CH_3 + CH_3OH$	3.97×10^4	7.11×10^8	1.45×10^4	−33.73	RN2, [33]
35	$CH_3 + CH_3 \longrightarrow C_2H_6$	0.00	1.00×10^4	-3.54×10^5	−176.05	RN2, [33]

of the n species present in the system. Each ODE is expressed as the algebraic sum of all relevant reaction rates (R_i) corresponding to a given reaction step, i.e. all rates that involve a given species. The reaction rate of each step is defined as $R_i = k_i \Pi_j C_j$, where k_i is defined by Eq. (1) and C_j is the concentration of the relevant species of step i. The microkinetic model and the governing ODEs for the change in species concentration are implemented in MATLAB [51].

2.3. Reaction systems

In this work, we consider two reaction networks (see Table 1). The first consists of 16 reactions proposed by Fernandes et al. [32] after experimental observations of DMC decomposition at relatively low temperatures, referred to as reaction network 1 (i.e. RN1 in Table 1). The second extends these 16 reactions to 35 using reactions from Sun et al. [33] who validated a network model for DMC pyrolysis at much higher temperatures. Hence, reaction network 2 (RN2) consists of those identified as RN1 and RN2. From Table 1 it can be seen that RN2 involves radical reactions unlike RN1. In RN2 the radicals are driven by the formation of CH_3 from DMC and H from CH_3O.

The initial conditions of the system set the DMC to have a concentration of 11.87 mol L^{-1} to replicate the experiment of Sun et al. [33]. It is assumed that the concentration of water in the sample is 1.3×10^{-3} mol L^{-1}. This is to represent the maximum contamination in commercially available DMC as Sun et al. [33] do not state a value for the H_2O content in their experiment. Initial concentrations of all other species are set to 0 mol L^{-1}. The theoretically estimated values of the forward step enthalpy and frequency factor determined from DFT analysis and transition state theory are presented in Table 1. Table 1 also presents the reaction enthalpy and entropy which is fixed throughout the optimisation. The reaction is considered to occur at a constant temperature of 300°C.

2.4. Optimisation procedure

The optimisation of the reaction network parameters (enthalpy of activation and pre-exponential factors) was carried out by minimising objective functions for each species present experimentally, as well as the value of DMC. The objective function of each species was given by the root mean square error between the predicted value and the experimental data points, considering all experimental data points. This was implemented in MATLAB using a genetic algorithm to find the Pareto front of the multiple objective functions. The experimental data used in the objective function is for the reaction of DMC at 180°C, 240°C and 300°C from the work by Fernandes et al. [32]. The enthalpy of activation, $H_f^{\ddagger}$, of the forward steps were optimised within the bounds of 25% either side of the initial value determined from DFT analysis. Similarly, the frequency factors, A_f, of the forward steps were optimised within the bounds of two orders of magnitude (larger and smaller) respective to the initial value determined from DFT analysis. The performance of RN1 and RN2 were both separately assessed in this way to determine if they appropriately represent the reaction system.

2.5. Reaction network analysis

The dominant reactions within the network are determined through net rate analysis and degree of rate control (DRC) analysis.

2.5.1. Net rate analysis

Net rate analysis provides information on the preferred mechanisms by which a reactant, i.e DMC, can form products [52]. Here it is used to identify the dominant reactions under different reaction temperature conditions, i.e. at temperatures of 280°C, 300°C and 320°C. After calculating the net rates under these conditions, a reaction network graph displaying the net rates is analysed, comparing parallel elementary

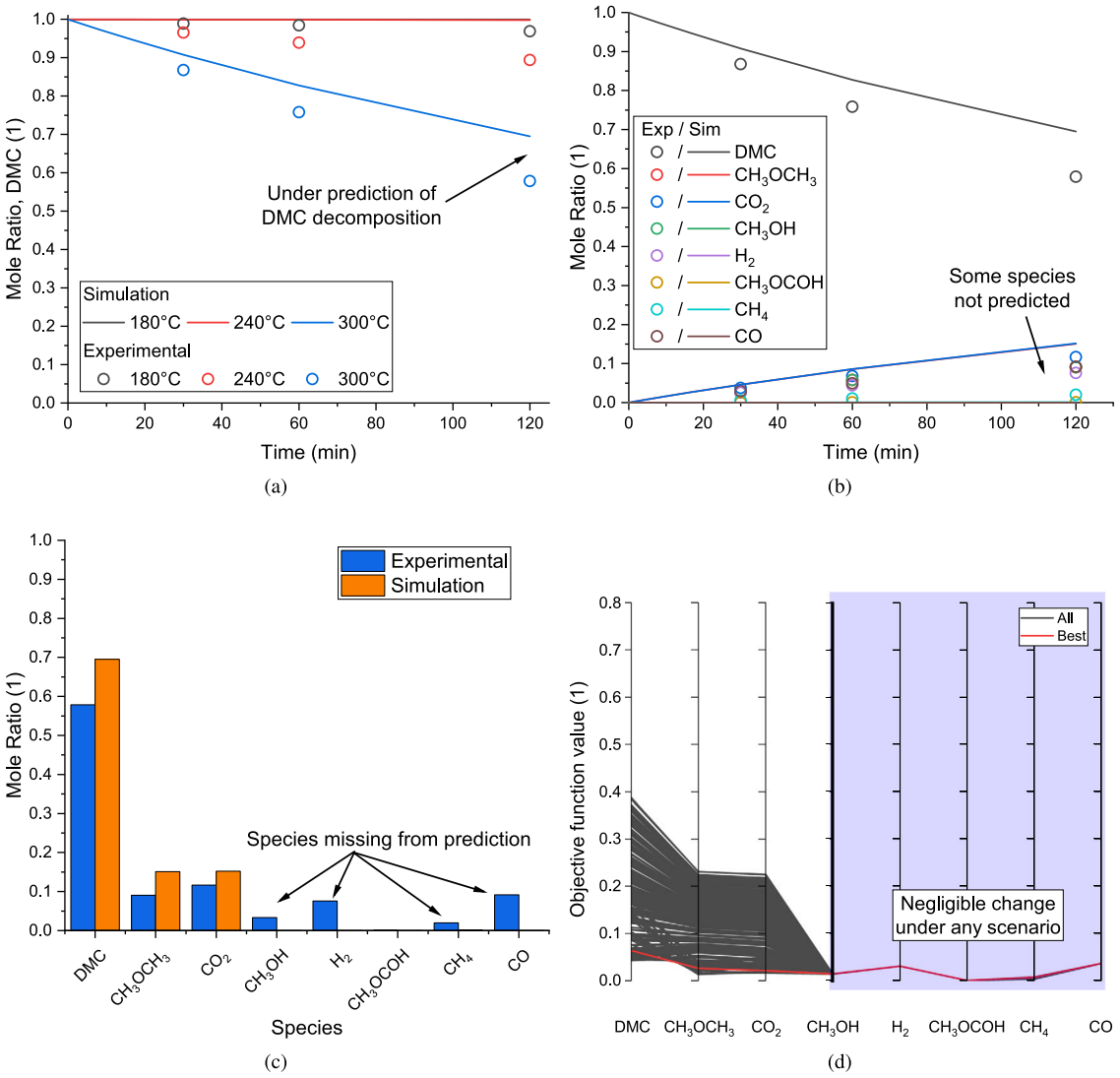

Fig. 1. RN1 optimisation results (a) DMC decomposition with time at different reaction temperatures (b) DMC decomposition and product generation at 300°C, (c) composition at $t = 120$ min at 300°C, and (d) values of the objective functions.
Source: Experimental results from Ref. [32].

steps, to determine the dominant pathway. In this work, analysis of the net rates is done at the point the DMC has decomposed by 10% for each temperature condition.

2.5.2. Degree of rate control analysis

The DRC is used to determine the kinetic importance of a given reaction step in the network [53]. This quantity is calculated by Eq. (10) for generation of a single species with an overall reaction rate r. The forward and backward rate constants (k) for step i is increased by 10%, while the equilibrium constant for step i and all other kinetic parameters for the other steps remain unchanged.

$$X_{rc,i} = \left(\frac{k_i}{r}\right)\left(\frac{\delta r}{\delta k_i}\right) \tag{10}$$

For a system with multiple products, the $X_{rc,i}$ can be summed over all products [54] according to Eq. (11). The rate of production of species n is given by r_n and the absolute value is used since a kinetic parameter may have both positive and negative sensitivities for different products.

$$\sum |X_{rc,i}| = \sum_n \left|\left(\frac{k_i}{r}\right)\left(\frac{\delta r_n}{\delta k_i}\right)\right| \tag{11}$$

From this, the reaction steps are ordered from the highest to the lowest DRC. Then the influence of the lowest steps can be analysed by removing them one at a time (starting with the lowest) and calculating the effect on the model output. This effect is quantified by the mean absolute percentage difference of all species mole fractions between the full reaction network and the reduced reaction network. When the effect is greater than a desirable amount, i.e. 1%, then network reduction stops. The removal of the reactions is done in an accumulative manner, such that the final reduced network consists of the full network minus the reactions removed up to the point before the 1% limit is first reached.

3. Results and discussion

3.1. Optimisation of kinetic parameters

The results from the optimisation of RN1 are presented in Fig. 1. The results shown relate to the "best" objective function, i.e that with the lowest overall value from the sum of the individual species objective functions. Fig. 1(a) shows a comparison between the experimental results and simulation predictions for DMC decomposition at different reaction temperatures. Fig. 1(b) presents a comparison of the predicted

Table 2
Optimised parameters for RN1 and RN2 from the "best" instance of the objective function, relating the figures plotted in Figs. 1 and 2.

Reaction	$\Delta H_f^{\ddagger}$ (J mol^{-1})			A_f (s^{-1}) or (L s^{-1} mol^{-1})		
	Original	Opt. RN1	Opt. RN2	Original	Opt. RN1	Opt. RN2
1	2.71×10^{5}	2.16×10^{5}	2.10×10^{5}	3.37×10^{14}	3.55×10^{15}	1.01×10^{15}
2	2.20×10^{5}	1.89×10^{5}	2.13×10^{5}	2.52×10^{10}	1.35×10^{11}	1.36×10^{11}
3	1.59×10^{5}	1.51×10^{5}	1.58×10^{5}	1.62×10^{14}	1.87×10^{14}	1.16×10^{14}
4	2.95×10^{5}	2.94×10^{5}	3.25×10^{5}	1.74×10^{10}	1.74×10^{10}	3.53×10^{10}
5	3.09×10^{5}	2.42×10^{5}	3.37×10^{5}	1.30×10^{15}	6.08×10^{16}	6.85×10^{14}
6	3.35×10^{5}	2.80×10^{5}	3.34×10^{5}	1.38×10^{14}	5.82×10^{13}	8.79×10^{14}
7	3.12×10^{5}	3.07×10^{5}	3.55×10^{5}	1.00×10^{10}	2.83×10^{9}	2.96×10^{10}
8	1.23×10^{5}	1.17×10^{5}	1.45×10^{5}	2.91×10^{5}	1.07×10^{6}	2.09×10^{5}
9	3.03×10^{5}	3.16×10^{5}	2.97×10^{5}	2.05×10^{15}	8.96×10^{14}	9.52×10^{14}
10	2.74×10^{5}	2.51×10^{5}	2.44×10^{5}	1.08×10^{15}	1.00×10^{15}	7.79×10^{14}
11	4.76×10^{5}	4.60×10^{5}	5.11×10^{5}	7.14×10^{13}	1.80×10^{14}	1.87×10^{14}
12	3.68×10^{5}	3.82×10^{5}	3.49×10^{5}	5.85×10^{13}	5.85×10^{13}	3.19×10^{13}
13	3.56×10^{5}	3.32×10^{5}	3.67×10^{5}	9.95×10^{13}	4.32×10^{13}	9.75×10^{13}
14	4.30×10^{5}	3.81×10^{5}	4.54×10^{5}	2.36×10^{14}	1.09×10^{14}	6.40×10^{14}
15	1.28×10^{5}	1.21×10^{5}	1.41×10^{5}	1.17×10^{14}	1.79×10^{14}	2.62×10^{14}
16	4.75×10^{5}	4.63×10^{5}	5.33×10^{5}	9.46×10^{10}	2.63×10^{10}	9.19×10^{10}
17	3.40×10^{5}	n/a	3.03×10^{5}	1.74×10^{14}	n/a	2.14×10^{15}
18	4.32×10^{4}	n/a	4.59×10^{4}	6.52×10^{9}	n/a	9.69×10^{8}
19	1.60×10^{4}	n/a	1.54×10^{4}	7.23×10^{9}	n/a	4.82×10^{9}
20	4.65×10^{4}	n/a	4.28×10^{4}	3.38×10^{14}	n/a	1.69×10^{14}
21	1.26×10^{5}	n/a	1.29×10^{5}	6.27×10^{14}	n/a	1.40×10^{14}
22	1.13×10^{5}	n/a	1.26×10^{5}	2.15×10^{14}	n/a	9.61×10^{13}
23	8.29×10^{4}	n/a	8.80×10^{4}	3.42×10^{14}	n/a	3.00×10^{15}
24	2.90×10^{3}	n/a	2.64×10^{3}	4.29×10^{11}	n/a	1.19×10^{11}
25	3.70×10^{4}	n/a	3.45×10^{4}	2.15×10^{10}	n/a	2.66×10^{11}
26	1.13×10^{5}	n/a	1.10×10^{5}	2.76×10^{14}	n/a	7.57×10^{14}
27	0.00	n/a	0.00	1.03×10^{11}	n/a	1.06×10^{11}
28	1.73×10^{4}	n/a	1.67×10^{4}	4.41×10^{11}	n/a	2.81×10^{11}
29	9.03×10^{4}	n/a	9.79×10^{4}	5.41×10^{14}	n/a	3.55×10^{14}
30	8.06×10^{4}	n/a	7.73×10^{4}	1.43×10^{8}	n/a	7.84×10^{7}
31	1.47×10^{5}	n/a	1.49×10^{5}	3.89×10^{6}	n/a	4.97×10^{7}
32	9.04×10^{4}	n/a	9.11×10^{4}	6.62×10^{14}	n/a	2.34×10^{14}
33	0.00	n/a	0.00	1.99×10^{11}	n/a	2.00×10^{11}
34	3.97×10^{4}	n/a	3.88×10^{4}	7.11×10^{8}	n/a	6.66×10^{8}
35	0.00	n/a	0.00	1.00×10^{4}	n/a	1.79×10^{4}

mole ratios to the experimental values over time for a reaction temperature of 300°C. For ease of interpretation, the mole ratios at the end time (120 min, 300°C) are presented in Fig. 1(c). Fig. 1(d) shows the objective function values for all outputs of the optimisation solver, where the best overall objective function is highlighted in red.

Fig. 1(a) shows that the model fails predict DMC decomposition at reaction temperatures of 180°C and 240°C, while at 300°C the rate of decomposition is slower than the experimental. Further, the decomposition of DMC only leads to CH_3OCH_3 and CO_2, see Figs. 1(b) and 1(c). The simulated quantity of CH_3OCH_3 and CO_2 is not greatly over predicted, with experimental mole ratio values of CH_3OCH_3 and CO_2 being 0.09 and 0.012 respectively compared to predictions of 0.15 for both species. However, it is clear that if the decomposition of DMC was greater there would be a greater production of CH_3OCH_3 and CO_2, and hence a greater error compared to the experimental. Predictions of the remaining off-gas species, CH_4, CH_3OH, H_2 and CO, are non existent.

Fig. 1(c) has shown that CH_4, CH_3OH, H_2 and CO are not present in the "best" solution. However, looking at Fig. 1(d) we can see that there is no significant change in the objective function values for these species at any point along the Pareto front. As such, it implies that (within the optimisation bounds) RN1 is not able to produce the experimentally detected species.

The values of the optimised parameters relating to the model predictions in Fig. 1 are presented in Table 2. The greatest change in reaction parameters corresponds to reactions 1, 2, 5 and 6. Reaction 1, the unimolecular decomposition of DMC, has a 20% reduction in activation energy and one order of magnitude increase in frequency factor. Reaction 2, the decomposition of DMC with water, has a 14% reduction in activation energy and one order of magnitude increase in frequency factor. However, there is a negligible change in the concentration of water compared to the initial conditions. This implies that this reaction does not proceed significantly. Reaction 5, the unimolecular decomposition of CH_3OCH_3, has a 22% reduction in activation energy and one order of magnitude increase in frequency factor. However, this still does not lead to the presence of CH_4. Reaction 6, the unimolecular decomposition of CH_2O, has a 16% reduction in activation energy. However. the enthalpy of activation is still high, 2.80×10^{5} J mol^{-1} compared to 2.16×10^{5} J mol^{-1} for Reaction 1. As such this reaction is kinetically unfavourable, hence H_2 and CO are not produced. From this analysis, the optimal solution of RN1 at this temperature adheres to the reaction scheme of Reaction 1.

As RN1 does not produce accurate predictions and fails to produce many of the species present in the experimental data, RN2 was optimised. The results for optimised RN2 are presented in Fig. 2. As with RN1 the results relate to the "best" total objective function value, see Table 2 for the optimised parameters for this solution.

Fig. 2(a) shows that RN2 with optimised parameters fails to predict DMC decomposition at reaction temperatures of 180°C and 240°C, similar to RN1. However, at 300°C RN2 accurately predicts the decomposition of DMC with a mole ratio of 0.6 verses an experimental value of 0.58 at the final time point, unlike RN1 with a predicted mole ratio of 0.7 at the same time. Along with the accurate predictions of DMC decomposition, Fig. 2(b) shows that the optimised RN2 network produces accurate predictions of species generation over the time investigated

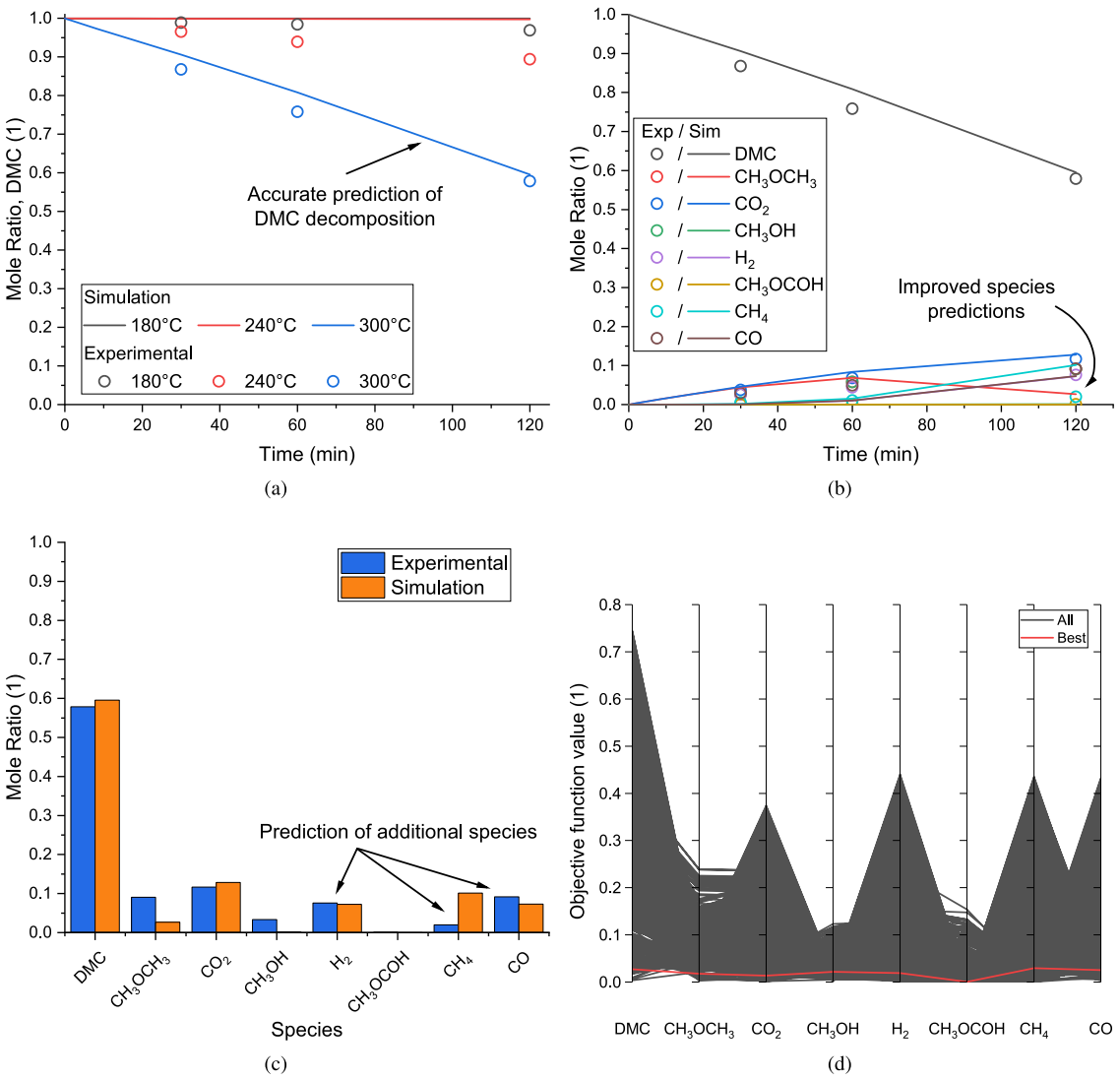

Fig. 2. RN2 optimisation results (a) DMC decomposition with time at different reaction temperatures (b) DMC decomposition and product generation at 300°C, (c) composition at $t = 120$ min for full network (at 300°C), and (d) values of the objective functions.
Source: Experimental results from Ref. [32].

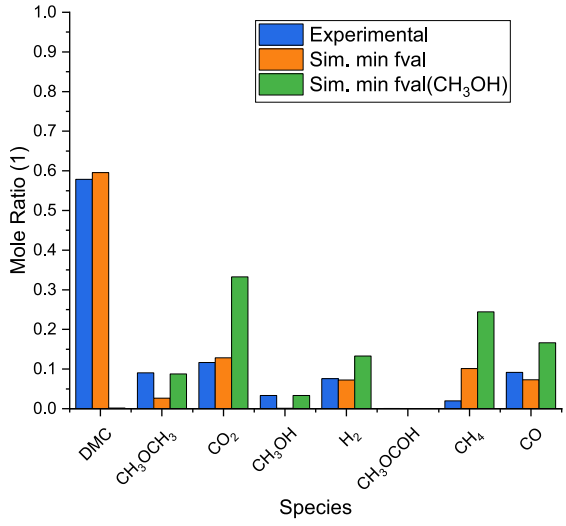

Fig. 3. Comparison of mole ratios at 120 min (under reaction temperature of 300°C) for solutions relating to the minimum total objective function and minimum CH_3OH objective function in reaction network 2..
Source: Experimental results from Ref. [32].

at a reaction temperature of 300°C. From Fig. 2(c) we see that RN2 predicts the generation of all species except CH_3OH, unlike RN1 which only predict CH_3OCH_3 and CO_2. Further, we see that the difference between the experimental and predicted mole ratios of CO_2, H_2 and CO are less than 0.02 in all cases. While there is an under prediction of CH_3OCH_3 (mole ratio of 0.03 predicted vs. experimental of 0.09) and an over prediction of CH_4 presumably due to the (indirect) conversion of CH_3OCH_3 to CH_4, H_2 and CO.

Although the generation of CH_3OH is not predicted in the "best" optimisation solution of RN2, the network does lead to the production of CH_3OH in many cases at various scales (as does CH_3OCOH). This can be seen from the values of the objective functions from the optimisation procedure in Fig. 2(d). Looking at the solution where the objective function for the CH_3OH species is minimal, see Fig. 3, it can be seen that the decomposition of DMC is complete. Further, there are significant differences in the mole ratios of the products species. From this, it is clear that there are competing schemes within the network (RN2) for the minimisation of the error of all species.

To compare the overall performance of the optimised networks of RN1 and RN2 the objective function values (calculated over the three experimental temperatures) of the "best" solutions are compared in Table 3. From this, it can be seen that for RN2 the decomposition of DMC and the generation of the products is predicted better, with

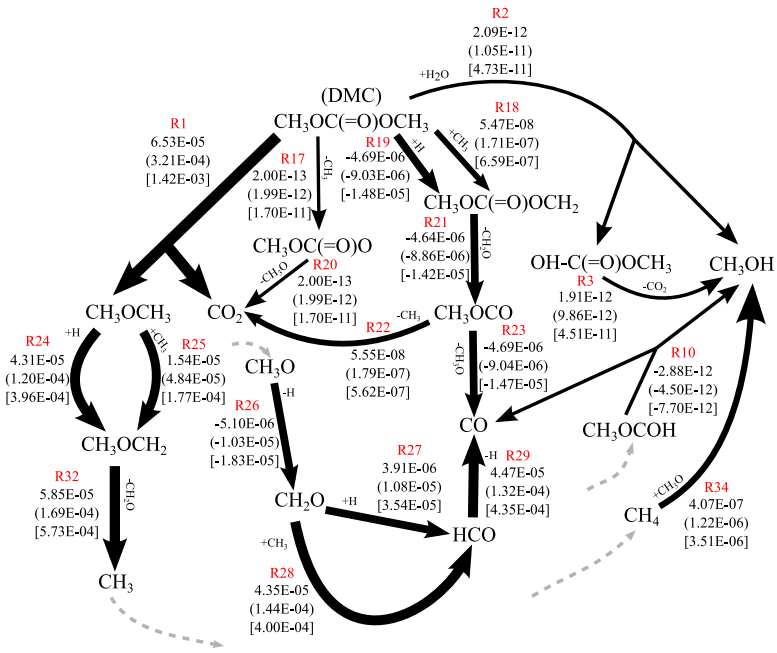

Fig. 4. Net rate analysis of RN2 at the point that DMC has decomposed to a mole fraction of 0.9. The rates of reaction in $\mathrm{mol\,L^{-1}\,s^{-1}}$ are given for reaction temperatures of 280°C, 300°C and 320°C identified by no, round and square brackets respectively. For clarity, reactions are also labelled in red according to the reaction number in Table 1. Arrows point in the forward direction, with positive rates indicating the net reaction is in the forward direction while negative rates indicate it is in the reverse direction. Grey dashed arrows indicate a generic generation/consumption reaction path that can be determined from the reaction list in Table 1.

Table 3
Comparison of objective function values calculated over the three experimental temperatures for the "best" cases.

	DMC	CH_3OCH_3	CO_2	CH_3OH	H_2	CH_3OCOH	CH_4	CO	Sum
RN1	0.0264	0.0213	0.0143	0.0309	0.0003	0.0072	0.0365	0.0639	0.2008
RN2	0.0258	0.0178	0.0140	0.0149	0.0003	0.0273	0.0182	0.0483	0.1666

lower objective functions throughout, than RN1. Note that the value of the fitness function of CH_3OCOH is greater in RN2. However, as the objective function aim is effectively zero for this species and the predicted values are effectively zero, the changes are insignificant. Overall error in RN2 is reduced by 17% compared to RN1.

As is shown above, the additional reactions in RN2 are necessary for the prediction of DMC decomposition and its off-gas species at 300°C. As such RN2 is further analysed to determine the importance of individual reactions, and in turn, those that may have no influence on the solution. This is discussed in the following section, Section 3.2.

3.2. Reaction network analysis

3.2.1. Net rate analysis

The results of the net rate analysis are presented in Fig. 4 for three reaction temperatures at the point DMC has decomposed by 10%. To reduce the complexity, Fig. 4 only shows the most important reactions with net rates of an order of $1 \times 10^{-12}\,\mathrm{mol\,L^{-1}\,s^{-1}}$ or greater (referenced against the initial net rate analysis at 300°C). Also, for clarity not all interlinks between species are shown. Hence, species CH_3, CH_3O, CH_3OCOH and CH_4 are not shown to be accurately generated/consumed in the figure. However, by looking at the arrows or the reaction list one can see that these species are produced/ consumed elsewhere in the network. For example, we can see CH_3 is consumed by R18 through the arrows depiction of + CH_3.

Fig. 4 indicates the greatest rate of CO_2 production is via R1 on an order of $1 \times 10^{-4}\,\mathrm{mol\,L^{-1}\,s^{-1}}$, then also via the sequence R18, R21 and R22 on the order of $1 \times 10^{-7}\,\mathrm{mol\,L^{-1}\,s^{-1}}$. R3 and R20 show a limited rate towards CO_2 production, while R9, R16 and R20 have rates lower than $1 \times 10^{-12}\,\mathrm{mol\,L^{-1}\,s^{-1}}$. The only reaction towards CH_3OCH_3 production is R1. The net rates towards CH_3OH production show reaction R4, R12 and R13 to be negligible, while R2, R3 and R10 are on the order of $1 \times 10^{-11}\,\mathrm{mol\,L^{-1}\,s^{-1}}$ to $1 \times 10^{-12}\,\mathrm{mol\,L^{-1}\,s^{-1}}$. In which R10 is in favour of the reverse direction. The rate towards CH_3OH production is dominated by R34 on the order of $1 \times 10^{-6}\,\mathrm{mol\,L^{-1}\,s^{-1}}$. For the production of H_2 only reaction R19, R24 and R27 are present in the net rate analysis of Fig. 4. In which R19 consumes H_2 at a rate on the order of $1 \times 10^{-6}\,\mathrm{mol\,L^{-1}\,s^{-1}}$, while reactions R24 and R30 produce CO_2 on the order of $1 \times 10^{-4}\,\mathrm{mol\,L^{-1}\,s^{-1}}$ and $1 \times 10^{-6}\,\mathrm{mol\,L^{-1}\,s^{-1}}$, respectively. CH_4 is produced via R18, R25 and R28 with a rate on the order of $1 \times 10^{-7}\,\mathrm{mol\,L^{-1}\,s^{-1}}$, $1 \times 10^{-5}\,\mathrm{mol\,L^{-1}\,s^{-1}}$ and $1 \times 10^{-4}\,\mathrm{mol\,L^{-1}\,s^{-1}}$ respectively. While it is consumed by R34 at a net rate of $1 \times 10^{-6}\,\mathrm{mol\,L^{-1}\,s^{-1}}$. Finally, CO is produced at a rate on the order of $1 \times 10^{-4}\,\mathrm{mol\,L^{-1}\,s^{-1}}$ via R29, but is consumed at a rate on the order of $1 \times 10^{-6}\,\mathrm{mol\,L^{-1}\,s^{-1}}$ by R23.

From this, and referring back to Fig. 2(c), it is clear that the generation of CH_3OCH_3 and CO_2 is dominated by R1. However, radical reactions are also important in the generation of CO_2. Also, it is only via pathways involving radical reactions that CH_3OCH_3 decomposes and leads to CO, CH_4 and H_2, and for CH_3OH generation.

As is expected, there is a decrease/increase of the reactions rates for the lower (280°C) and higher (320°C) temperatures, respectively. However, there is no significant change in network dynamics between the three cases; hence, the conclusions made above hold for these temperatures as well.

3.2.2. Degree of rate control analysis

The DRC of each reaction was calculated according the methods in Section 2.5.2. While the DRC was calculated at all time points, analysis is carried out at the first instance of the simulation (specifically 5×10^{-4} s). The results of the DRC analysis are presented in Table 4. From this we can see that R17, the removal of a CH_3 radical from DMC, is the most rate controlling with a DRC value of 18.37. This

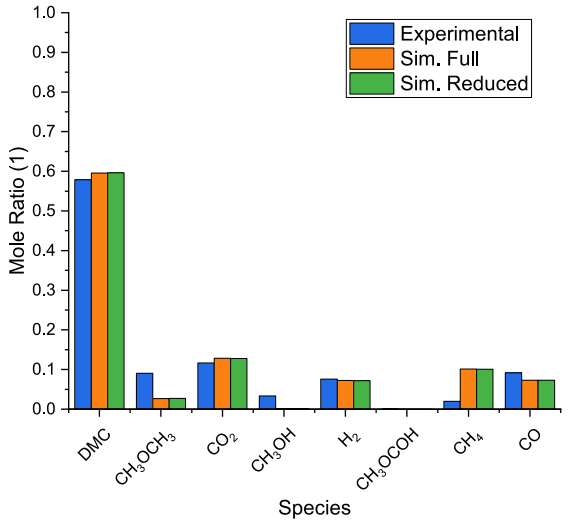

Fig. 5. Comparison of mole ratios at 120 min (under reaction temperature of 300°C) for the original solution relating to the minimum total objective function in reaction network 2 and the solution from the reaction network reduced in size following degree of rate control analysis.
Source: Experimental results from Ref. [32].

is followed by R21, R1 and R18, with DRC values on the scale of 6, and are the reactions of $CH_3OCOOCH_2$ decomposing to CH_3OCO, the direct decomposition of DMC to dimethyl ether and CO_2, and finally the reaction of DMC with a methyl radical, respectively.

Comparing the reactions of greatest DRC (R17, R21, R1, R18) to the net rate analysis in Fig. 4, we see that R1 has the greatest net rate on the scale of 1×10^{-4} mol L^{-1} s^{-1} (at 300°C) compared to 1×10^{-12} mol L^{-1} s^{-1} and 1×10^{-7} mol L^{-1} s^{-1} for R17 and R18 respectively. While the greatest rate of decomposition is via R1, DRC shows that R17 and R18 are critical for the overall decomposition of DMC.

The results of Table 4 are also used to identify which reactions are least controlling and in-turn negligible on prediction output, such that they can be omitted from the reaction network (RN2). By consecutively and accumulatively removing reactions from the network, from least rate controlling upwards, a reduced network of RN2 is determined. In this way it is shown that reactions 3, 8, 9, 10, 11, 12, 13, 14, 16, 22, 30 and 31 can be removed with negligible effect on the output, i.e. there is only a difference of 0.48% between the full and reduced network, see Fig. 5. Further removal of reactions 34, 7, 5 and 6 leads to a difference between the full and reduced network of 6.61%, 6.36% 7.03%, and 6.32% respectively. Comparing the reactions that have been removed to the net rate analysis in Fig. 4, we can see that only reaction R3 and R22 are present in the figure. As such there is a clear corroboration of the analysis methods to identify redundant reactions.

Further to this, the DRC and the assessment of the reduced network at the same temperatures as in the net rate analysis, i.e 280°C and 320°C, is also investigated. At all three temperature, DRC identifies reactions 8, 9, 10, 11, 12, 14, 16, 30 and 31 to have negligible rate control. Compared to 300°C, which also identifies reactions 3, 13 and 22 to be negligible, at 280°C its reactions 6, 7 and 34, and at 320°C it is reactions 5, 5 and 22 that are also negligible. At 280°C and 320°C, using the reduced network determined via DRC analysis at 300°C, the difference between the full and reduced networks is 0% and 1.22%, respectively. Indicating the reduced model is appropriate for temperatures away from that used for the main DRC analysis. Further, to determine the upper reaction temperature that the reduced model can be used a comparison is made at 600°C. Here, the difference between the full and reduced model is 4.36%, as such there is a limit to the accuracy of the reduced model above 600°C. A table of the DRC analysis and figures for the comparison at these temperatures is supplied in *Supplementary Material A*, Table A1 and figures Figure A1 to Figure A3.

Table 4
The DRC for each reaction (R №) summed over all products, $\sum|X_{rc,i}|$, at the start of the simulation ($t = 5\times10^{-4}$ s) for a reaction temperature of 300°C. Reactions are ordered from most the least rate determining.

R №	DRC	R №	DRC	R №	DRC
17	18.37	29	1.46	22	0.17
21	6.66	33	1.18	3	0.00
1	6.38	35	1.00	10	0.00
18	6.05	4	1.00	8	0.00
2	3.40	15	0.59	9	0.00
26	3.19	20	0.58	11	0.00
19	2.15	27	0.56	12	0.00
25	2.08	6	0.56	14	0.00
23	1.84	7	0.56	16	0.00
32	1.73	5	0.56	30	0.00
28	1.55	34	0.56	31	0.00
24	1.48	13	0.41		

Comparing reactions with a large change in kinetic parameter values due to optimisation (see Table 2) to the degree of rate control analysis it can be seen that the large change in parameters for reactions 8, 10, 16, 22, 30 and 31 correspond to reactions with a limited degree of control. Hence, the changes in these reaction parameters during optimisation probably carried little weight to the optimised solution.

The limit of DMC decomposition onset is determined by simulating a linear increase in temperate, see Fig. 6(a). From this it can be see that decomposition begins in the range of 250°C to 300°C. While the model does not fully address the behaviour seen in the experimental tests by [32] used in this work, it identifies that decomposition can occur at relatively low temperatures and that the lack of decomposition in the experimental by [28] needs to be further understood.

Also from Fig. 6(a) we plot a parity plot of the DMC decomposition between the full and reduced reaction networks in Fig. 6(b). From the we can see the straight line fit of the plot has a high R^2 value (0.99995), and that the deviation of parity points away from the $y = x$ line is less than 5% at most. Hence, the reduced model can be used across the entire temperature range DMC decomposition occurs.

4. Conclusion

Although an essential energy storage device, LIBs are hazardous as they can undergo the complex chemical process of thermal runaway due to the decomposition of the cell's components. Modelling of this process aids the understanding of its behaviours and the design of safer batteries. However, the models that are currently implemented do not consider the fundamental reactions taking place, and as such do not allow for the prediction of off-gas species. As such we have applied micro-kinetic modelling to be able to simulate the mechanistic behaviour of Li-ion battery thermal runaway.

We focused on producing a micro-kinetic model for the thermal decomposition of DMC, an important electrolyte component. For this, two reaction networks were investigated, the first did not involve radical pathways, while the second involved radicals driven by the formation of CH_3 from DMC and H from CH_3O. Through optimisation of kinetic parameters where initial conditions were determined from DFT calculations, it was shown the first reaction network did not predict the decomposition of DMC accurately nor accurately predicted the off-gas species'. However, the second network improved predictions of off-gas species', and reduced the error by 17%. Further, degree of rate control analysis was applied the second network to determine the rate controlling and negligible steps. With this, the second reaction network was reduced as 12 of the reactions were determined to have minimal effect on the system.

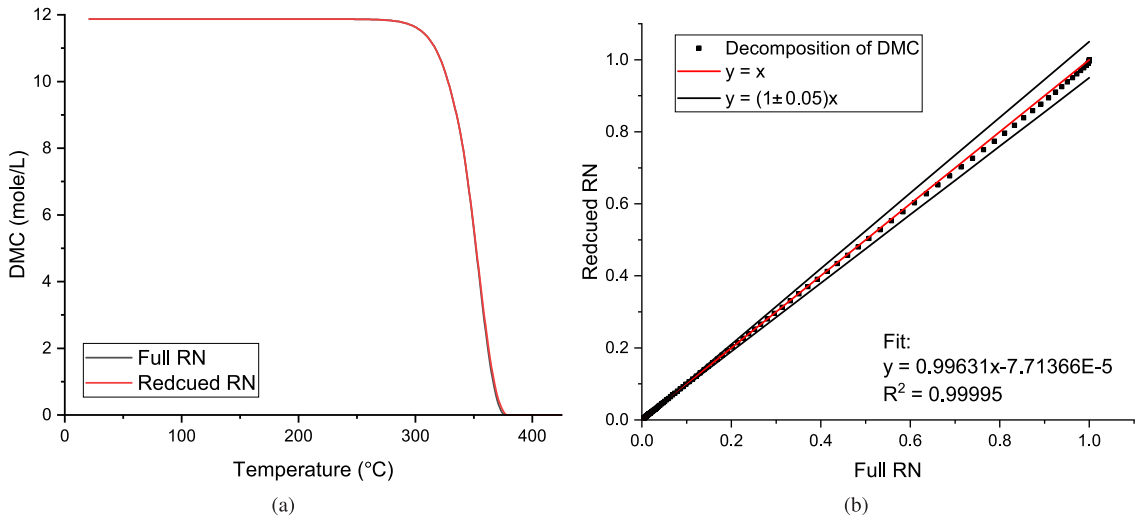

Fig. 6. (a) Decomposition of DMC given a linear increase in temperature. Predicted according to the full RN2 and the reduced RN2 models. (b) Parity plot of DMC decomposition from (a) where 0 is no decomposition and 1 is full decomposition.

This work makes it possible to predict the production of hazardous species and the causal pathways of individual species, enabling the design of safer Li-ion cells from a mechanistic level. It also allows for quantities such as lower flammability limit and heat generation to be determined, providing extended predictive capabilities that can be utilised in the risk assessment of LIB energy storage systems. However, to be practical for LIB researchers/developers future work needs to incorporate the reaction systems of all the Li-ion cell's components, i.e. all electrolyte and electrode materials. Being there are contradictory experimental results for the decomposition of DMC as highlighted in the literature review, reliable experiential data for the decomposition of individual components is also needed for robust optimisation and validation of reaction networks.

CRediT authorship contribution statement

Peter J. Bugryniec: Conceptualization, Methodology, Software, Visualization, Writing – original draft. **Sergio Vernuccio:** Methodology, Writing – review & editing. **Solomon F. Brown:** Supervision, Writing – review & editing.

Declaration of competing interest

The authors declare that they have no known competing financial interests or personal relationships that could have appeared to influence the work reported in this paper.

Data availability

Data will be made available on request.

Acknowledgment

This work was supported by the Faraday Institution.

Appendix A. Supplementary data

Supplementary material related to this article can be found online at https://doi.org/10.1016/j.jpowsour.2023.233394.

References

[1] D. Deng, Li-ion batteries: basics, progress, and challenges, Energy Sci. Eng. 3 (5) (2015) 385–418, http://dx.doi.org/10.1002/ese3.95, arXiv:https://onlinelibrary.wiley.com/doi/pdf/10.1002/ese3.95. URL https://onlinelibrary.wiley.com/doi/abs/10.1002/ese3.95.

[2] M.S. Ziegler, J.E. Trancik, Re-examining rates of lithium-ion battery technology improvement and cost decline, Energy Environ. Sci. 14 (2021) 1635–1651, http://dx.doi.org/10.1039/D0EE02681F.

[3] E.A. Kapp, D.S. Wroth, J.T. Chapin, Analysis of thermal runaway incidents involving lithium batteries in U.S. commercial aviation, Transp. Res. Rec. 2674 (11) (2020) 584–592, http://dx.doi.org/10.1177/0361198120947711, arXiv:https://doi.org/10.1177/0361198120947711.

[4] R. Zalosh, P. Gandhi, A. Barowy, Lithium-ion energy storage battery explosion incidents, J. Loss Prev. Process Ind. 72 (2021) 104560, http://dx.doi.org/10.1016/j.jlp.2021.104560, URL https://www.sciencedirect.com/science/article/pii/S0950423021001686.

[5] Y.-S. Duh, Y. Sun, X. Lin, J. Zheng, M. Wang, Y. Wang, X. Lin, X. Jiang, Z. Zheng, S. Zheng, G. Yu, Characterization on thermal runaway of commercial 18650 lithium-ion batteries used in electric vehicles: A review, J. Energy Storage 41 (2021) 102888, http://dx.doi.org/10.1016/j.est.2021.102888, URL https://www.sciencedirect.com/science/article/pii/S2352152X21006095.

[6] Q. Wang, P. Ping, X. Zhao, G. Chu, J. Sun, C. Chen, Thermal runaway caused fire and explosion of lithium ion battery, J. Power Sources 208 (2012) 210–224, http://dx.doi.org/10.1016/j.jpowsour.2012.02.038, URL https://www.sciencedirect.com/science/article/pii/S0378775312003989.

[7] Q. Wang, B. Mao, S.I. Stoliarov, J. Sun, A review of lithium ion battery failure mechanisms and fire prevention strategies, Prog. Energy Combust. Sci. 73 (2019) 95–131, http://dx.doi.org/10.1016/j.pecs.2019.03.002, URL https://www.sciencedirect.com/science/article/pii/S0360128518301801.

[8] P.J. Bugryniec, J.N. Davidson, D.J. Cumming, S.F. Brown, Pursuing safer batteries: Thermal abuse of $LiFePO_4$ cells, J. Power Sources 414 (2019) 557–568, http://dx.doi.org/10.1016/j.jpowsour.2019.01.013.

[9] R. Spotnitz, J. Franklin, Abuse behavior of high-power, lithium-ion cells, J. Power Sources 113 (1) (2003) 81–100, http://dx.doi.org/10.1016/S0378-7753(02)00488-3, URL https://www.sciencedirect.com/science/article/pii/S0378775302004883.

[10] G.H. Kim, A. Pesaran, R. Spotnitz, A three-dimensional thermal abuse model for lithium-ion cells, J. Power Sources 170 (2) (2007) 476–489, http://dx.doi.org/10.1016/j.jpowsour.2007.04.018.

[11] P.J. Bugryniec, J.N. Davidson, S.F. Brown, Advanced abuse modelling of Li-ion cells – A novel description of cell pressurisation and simmering reactions, J. Power Sources 474 (2020) 228396, http://dx.doi.org/10.1016/j.jpowsour.2020.228396, URL http://www.sciencedirect.com/science/article/pii/S037877532030700X.

[12] J.K. Ostanek, W. Li, P.P. Mukherjee, K. Crompton, C. Hacker, Simulating onset and evolution of thermal runaway in Li-ion cells using a coupled thermal and venting model, Appl. Energy 268 (2020) 114972, http://dx.doi.org/10.1016/j.apenergy.2020.114972, URL https://www.sciencedirect.com/science/article/pii/S0306261920304840.

[13] D. Mishra, K. Shah, A. Jain, Investigation of the impact of flow of vented gas on propagation of thermal runaway in a Li-ion battery pack, J. Electrochem. Soc. 168 (6) (2021) 060555, http://dx.doi.org/10.1149/1945-7111/ac0a20.

[14] J. Kim, A. Mallarapu, D.P. Finegan, S. Santhanagopalan, Modeling cell venting and gas-phase reactions in 18650 lithium ion batteries during thermal runaway, J. Power Sources 489 (2021) 229496, http://dx.doi.org/10.1016/j.jpowsour.2021.229496, URL https://www.sciencedirect.com/science/article/pii/S0378775321000458.

[15] D. Kong, G. Wang, P. Ping, J. Wen, A coupled conjugate heat transfer and CFD model for the thermal runaway evolution and jet fire of 18650 lithium-ion battery under thermal abuse, eTransportation 12 (2022) 100157, http://dx.doi.org/10.1016/j.etran.2022.100157, URL https://www.sciencedirect.com/science/article/pii/S2590116822000030.

[16] J. Pfaendtner, L.J. Broadbelt, Mechanistic modeling of lubricant degradation. 1. Structure-reactivity relationships for free-radical oxidation, Ind. Eng. Chem. Res. 47 (9) (2008) 2886–2896, http://dx.doi.org/10.1021/ie0714807, arXiv:https://doi.org/10.1021/ie0714807.

[17] J. Pfaendtner, X. Yu, L.J. Broadbelt, Quantum chemical investigation of low-temperature intramolecular hydrogen transfer reactions of hydrocarbons, J. Phys. Chem. A 110 (37) (2006) 10863–10871, http://dx.doi.org/10.1021/jp061649e, PMID: 16970383. arXiv:https://doi.org/10.1021/jp061649e.

[18] S. Vernuccio, E.E. Bickel, R. Gounder, L.J. Broadbelt, Microkinetic model of propylene oligomerization on brønsted acidic zeolites at low conversion, ACS Catal. 9 (10) (2019) 8996–9008, http://dx.doi.org/10.1021/acscatal.9b02066, arXiv:https://doi.org/10.1021/acscatal.9b02066.

[19] P.J. Bugryniec, A. Yeardley, A. Jain, N. Price, S. Vernuccio, S.F. Brown, Gaussian-Process based inference of electrolyte decomposition reaction networks in Li-ion battery failure, in: L. Montastruc, S. Negny (Eds.), 32nd European Symposium on Computer Aided Process Engineering, in: Computer Aided Chemical Engineering, vol. 51, Elsevier, 2022, pp. 157–162, http://dx.doi.org/10.1016/B978-0-323-95879-0.50027-8, URL https://www.sciencedirect.com/science/article/pii/B9780323958790500278.

[20] K. Xu, Nonaqueous liquid electrolytes for lithium-based rechargeable batteries, Chem. Rev. 104 (10) (2004) 4303–4418, http://dx.doi.org/10.1021/cr030203g, arXiv:https://doi.org/10.1021/cr030203g.

[21] G.M. Ehrlich, Lithium-ion batteries, in: D. Linden, T.B. Reddy (Eds.), Handbook of Batteries, third ed., McGraw-Hill, New York, 2002, Ch. 35.

[22] N.P. Lebedeva, L. Boon-Brett, Considerations on the chemical toxicity of contemporary Li-ion battery electrolytes and their components, J. Electrochem. Soc. 163 (6) (2016) A821–A830, http://dx.doi.org/10.1149/2.0171606jes.

[23] S. Nowak, M. Winter, The role of sub- and supercritical CO2 as “processing solvent” for the recycling and sample preparation of lithium ion battery electrolytes, Molecules 22 (3) (2017) http://dx.doi.org/10.3390/molecules22030403, URL https://www.mdpi.com/1420-3049/22/3/403.

[24] P. Balakrishnan, R. Ramesh, T. Prem Kumar, Safety mechanisms in lithium-ion batteries, J. Power Sources 155 (2) (2006) 401–414, http://dx.doi.org/10.1016/j.jpowsour.2005.12.002, URL https://www.sciencedirect.com/science/article/pii/S0378775305016629.

[25] E.P. Roth, C.J. Orendorff, How electrolytes influence battery safety, Interface Mag. 21 (2) (2012) 45–49, http://dx.doi.org/10.1149/2.f04122if.

[26] P. Ribière, S. Grugeon, M. Morcrette, S. Boyanov, S. Laruelle, G. Marlair, Investigation on the fire-induced hazards of Li-ion battery cells by fire calorimetry, Energy Environ. Sci. 5 (2012) 5271–5280, http://dx.doi.org/10.1039/C1EE02218K.

[27] A.S. Gordon, W.P. Norris, A study of the pyrolysis of methyl ethyl and diethyl carbonates in the gas phase, J. Phys. Chem. 69 (9) (1965) 3013–3017, http://dx.doi.org/10.1021/j100893a032, arXiv:https://doi.org/10.1021/j100893a032.

[28] J. Lamb, C.J. Orendorff, E.P. Roth, J. Langendorf, Studies on the thermal breakdown of common Li-ion battery electrolyte components, J. Electrochem. Soc. 162 (10) (2015) A2131–A2135, http://dx.doi.org/10.1149/2.0651510jes.

[29] M.H.J. Wijnen, Decomposition of dimethyl carbonate on quartz, J. Chem. Phys. 34 (4) (1961) 1465–1466, http://dx.doi.org/10.1063/1.1731779, arXiv:https://doi.org/10.1063/1.1731779.

[30] J.C.J. Thynne, P. Gray, The methyl-radical-sensitized decomposition of gaseous dimethyl carbonate, Trans. Faraday Soc. 58 (1962) 2403–2409, http://dx.doi.org/10.1039/TF9625802403.

[31] M.J.Y. Quee, J.C.J. Thynne, Photolysis of dimethyl carbonate, Trans. Faraday Soc. 62 (1966) 3154–3161, http://dx.doi.org/10.1039/TF9666203154.

[32] Y. Fernandes, A. Bry, S. de Persis, Thermal degradation analyses of carbonate solvents used in Li-ion batteries, J. Power Sources 414 (2019) 250–261, http://dx.doi.org/10.1016/j.jpowsour.2018.12.077, URL https://www.sciencedirect.com/science/article/pii/S0378775318314289.

[33] W. Sun, B. Yang, N. Hansen, C.K. Westbrook, F. Zhang, G. Wang, K. Moshammer, C.K. Law, An experimental and kinetic modeling study on dimethyl carbonate (DMC) pyrolysis and combustion, Combust. Flame 164 (2016) 224–238, http://dx.doi.org/10.1016/j.combustflame.2015.11.019, URL https://www.sciencedirect.com/science/article/pii/S0010218015004137.

[34] K. Kanayama, S. Takahashi, S. Morikura, H. Nakamura, T. Tezuka, K. Maruta, Study on oxidation and pyrolysis of carbonate esters using a micro flow reactor with a controlled temperature profile. Part I: Reactivities of dimethyl carbonate, ethyl methyl carbonate and diethyl carbonate, Combust. Flame 237 (2022) 111810, http://dx.doi.org/10.1016/j.combustflame.2021.111810, URL https://www.sciencedirect.com/science/article/pii/S0010218021005538.

[35] S.L. Peukert, R. Sivaramakrishnan, J.V. Michael, High temperature shock tube and theoretical studies on the thermal decomposition of dimethyl carbonate and its bimolecular reactions with H and D-atoms, J. Phys. Chem. A 117 (18) (2013) 3718–3728, http://dx.doi.org/10.1021/jp312643k, PMID: 23510116. arXiv:https://doi.org/10.1021/jp312643k.

[36] P.A. Glaude, W.J. Pitz, M.J. Thomson, Chemical kinetic modeling of dimethyl carbonate in an opposed-flow diffusion flame, Proc. Combust. Inst. 30 (1) (2005) 1111–1118, http://dx.doi.org/10.1016/j.proci.2004.08.096, URL https://www.sciencedirect.com/science/article/pii/S0082078404001493.

[37] L. Xing, W. Li, C. Wang, F. Gu, M. Xu, C. Tan, J. Yi, Theoretical investigations on oxidative stability of solvents and oxidative decomposition mechanism of ethylene carbonate for lithium ion battery use, J. Phys. Chem. B 113 (52) (2009) 16596–16602, http://dx.doi.org/10.1021/jp9074064, arXiv:https://doi.org/10.1021/jp9074064.

[38] Y.-K. Han, S.U. Lee, Performance of density functionals for calculation of reductive ring-opening reaction energies of Li^+-EC and Li^+-VC, Theor. Chem. Acc. 112 (2) (2004) 106–112, http://dx.doi.org/10.1007/s00214-004-0572-5.

[39] Y. Wang, P.B. Balbuena, Theoretical insights into the reductive decompositions of propylene carbonate and vinylene carbonate: Density functional theory studies, J. Phys. Chem. B 106 (17) (2002) 4486–4495, http://dx.doi.org/10.1021/jp014371t.

[40] K. Tasaki, K. Kanda, S. Nakamura, M. Ue, Decomposition of $LiPF_6$ and stability of PF_5 in Li-ion battery electrolytes, J. Electrochem. Soc. 150 (12) (2003) A1628, http://dx.doi.org/10.1149/1.1622406.

[41] H. Hirai, R. Jinnouchi, Discovering chemical reaction pathways using accelerated molecular dynamics simulations and network analysis tools – Application to oxidation induced decomposition of ethylene carbonate, Chem. Phys. Lett. 770 (2021) 138439, http://dx.doi.org/10.1016/j.cplett.2021.138439, URL https://www.sciencedirect.com/science/article/pii/S0009261421001226.

[42] E. Hu, Y. Chen, Z. Zhang, L. Pan, Q. Li, Y. Cheng, Z. Huang, Experimental and kinetic study on ignition delay times of dimethyl carbonate at high temperature, Fuel 140 (2015) 626–632, http://dx.doi.org/10.1016/j.fuel.2014.10.013, URL https://www.sciencedirect.com/science/article/pii/S0016236114010059.

[43] K. Alexandrino, M.U. Alzueta, H.J. Curran, An experimental and modeling study of the ignition of dimethyl carbonate in shock tubes and rapid compression machine, Combust. Flame 188 (2018) 212–226, http://dx.doi.org/10.1016/j.combustflame.2017.10.001, URL https://www.sciencedirect.com/science/article/pii/S001021801730384X.

[44] M.J. Frisch, G.W. Trucks, H.B. Schlegel, G.E. Scuseria, M.A. Robb, J.R. Cheeseman, G. Scalmani, V. Barone, G.A. Petersson, H. Nakatsuji, X. Li, M. Caricato, A.V. Marenich, J. Bloino, B.G. Janesko, R. Gomperts, B. Mennucci, H.P. Hratchian, J.V. Ortiz, A.F. Izmaylov, J.L. Sonnenberg, D. Williams-Young, F. Ding, F. Lipparini, F. Egidi, J. Goings, B. Peng, A. Petrone, T. Henderson, D. Ranasinghe, V.G. Zakrzewski, J. Gao, N. Rega, G. Zheng, W. Liang, M. Hada, M. Ehara, K. Toyota, R. Fukuda, J. Hasegawa, M. Ishida, T. Nakajima, Y. Honda, O. Kitao, H. Nakai, T. Vreven, K. Throssell, J.A. Montgomery, J.E. Peralta Jr., F. Ogliaro, M.J. Bearpark, J.J. Heyd, E.N. Brothers, K.N. Kudin, V.N. Staroverov, T.A. Keith, R. Kobayashi, J. Normand, K. Raghavachari, A.P. Rendell, J.C. Burant, S.S. Iyengar, J. Tomasi, M. Cossi, J.M. Millam, M. Klene, C. Adamo, R. Cammi, J.W. Ochterski, R.L. Martin, K. Morokuma, O. Farkas, J.B. Foresman, D.J. Fox, Gaussian 16, Revision C.01, Gaussian, Inc., Wallingford CT, 2019, URL https://gaussian.com/gaussian16/.

[45] E.G. Leggesse, J.-C. Jiang, Theoretical study of the reductive decomposition of 1,3-propane sultone: SEI forming additive in lithium-ion batteries, RSC Adv. 2 (2012) 5439–5446, http://dx.doi.org/10.1039/C2RA20200J.

[46] E.G. Leggesse, R.T. Lin, T.-F. Teng, C.-L. Chen, J.-C. Jiang, Oxidative decomposition of propylene carbonate in lithium ion batteries: A DFT study, J. Phys. Chem. A 117 (33) (2013) 7959–7969, http://dx.doi.org/10.1021/jp403436u, arXiv:https://doi.org/10.1021/jp403436u.

[47] P. Zhang, S. Li, Y. Wang, W. Ji, W. Sun, B. Yang, X. He, Z. Wang, C.K. Law, F. Zhang, Measurement of reaction rate constants using RCM: A case study of decomposition of dimethyl carbonate to dimethyl ether, Combust. Flame 183 (2017) 30–38, http://dx.doi.org/10.1016/j.combustflame.2017.05.006, URL https://www.sciencedirect.com/science/article/pii/S0010218017301736.

[48] P.J. Robinson, Dimensions and standard states in the activated complex theory of reaction rates, J. Chem. Educ. 55 (8) (1978) 509, http://dx.doi.org/10.1021/ed055p509, arXiv:https://doi.org/10.1021/ed055p509.

[49] I. Filot, Introduction to Microkinetic Modeling, Eindhoven University of Technology, 2022, pp. 209–237, Ch. The Rates of Elementary Reaction Steps, Version 1.8.1. URL https://research.tue.nl/en/publications/introduction-to-microkinetic-modeling-2.

[50] R. Cortright, J. Dumesic, Kinetics of heterogeneous catalytic reactions: Analysis of reaction schemes, in: Advances in Catalysis, vol. 46, Academic Press, 2001, pp. 161–264, http://dx.doi.org/10.1016/S0360-0564(02)46023-3, URL https://www.sciencedirect.com/science/article/pii/S0360056402460233.

[51] MATLAB, Version 9.10.0 (R2021a), The MathWorks Inc., Natick, Massachusetts, 2021.

[52] L.D. Dellon, C.-Y. Sung, D.J. Robichaud, L.J. Broadbelt, 110Th anniversary: Microkinetic modeling of the vapor phase upgrading of biomass-derived oxygenates, Ind. Eng. Chem. Res. 58 (33) (2019) 15173–15189, http://dx.doi.org/10.1021/acs.iecr.9b03242, arXiv:https://doi.org/10.1021/acs.iecr.9b03242.

[53] C.T. Campbell, Future Directions and Industrial Perspectives Micro- and macro-kinetics: Their relationship in heterogeneous catalysis, Top. Catalysis 1 (3) (1994) 353–366, http://dx.doi.org/10.1007/BF01492288.

[54] M.A. Sanchez-Castillo, N. Agarwal, C. Miller, R.D. Cortright, R.J. Madon, J. Dumesic, Reaction kinetics study and analysis of reaction schemes for isobutane conversion over USY zeolite, J. Catalysis 205 (1) (2002) 67–85, http://dx.doi.org/10.1006/jcat.2001.3419, URL https://www.sciencedirect.com/science/article/pii/S0021951701934190.